Highlighting research from the Fluid & Interface Laboratory from the group of Prof. Hyoungsoo Kim.
Uniform coating pattern of evaporating multi-component liquid droplets in a confined geometry

Controlling uniform patterns by evaporation of multi-component liquid droplets in a confined geometry

A drying multi-component liquid droplet in a confined geometry leaves a uniform dried pattern. The evaporated vapors are stagnated inside the closed chamber, which induce Marangoni effects that contribute to suppress the coffee-ring pattern and achieve the uniform deposits. This technique can be applied to a perfectly uniform quantum dots (QDs) for a light-emitting layer.

ROYAL SOCIETY OF CHEMISTRY

rsc.li/soft-matter-journal

PAPER

Check for updates

Controlling uniform patterns by evaporation of multi-component liquid droplets in a confined geometry†

Jeongsu Pyeon and Hyoungsoo Kim ꙮ *

Surface-coating technologies are important for a variety of applications, *e.g.* ink-jet printing, microelectronic engineering and biological arrays. In this study, we introduce a novel idea to obtain uniform patterns with multi-component solution in a confined geometry. When a droplet of the multi-component liquid evaporates in the confined area, the evaporated vapors are stagnated inside the confined chamber where the evaporated liquid molecule is much heavier than the ambient air. These vapors change internal flow in the droplet by generating Marangoni effects during evaporation, which help to obtain uniform deposition. Finally, we show that a coffee-ring is totally suppressed and a uniformly dried pattern is achieved. For a potential application as display panels, we use quantum dots and create a uniform light-emitting layer.

1 Introduction

Understanding of the evaporation mechanism of a particle-laden droplet is crucial to control a final dried pattern, which has been receiving enormous attention in coating and electronics industries. The uniform coating results can be useful for various applications, such as light-emitting diode (LED) displays, electronic wiring, biological engineering for tissues and vasculature and radio-frequency identification (RFID).[1–7] In particular, the maximum illumination efficiency of LEDs can be increased by improving the thickness uniformity of the LED layer.[8,9] Also, the resistivity of the electronic wiring can be optimized when the printed electronic pattern has uniform morphology.[4] Furthermore, uniform conductive patterns can contribute to long-term stability for the performance of an electronic device such as RFID.[10]

To date, diverse deposition patterns were observed under different drying conditions, *e.g.*, coffee-ring patterns,[11] dual-ring patterns,[12,13] multiple ring patterns[13,14] and uniform patterns,[15–25] after a droplet was completely evaporated. The coffee-ring pattern is commonly observed from the evaporation of a single liquid component droplet with a low contact angle ($<90°$) where the evaporatively driven capillary flow occurs. If the contact line is pinned, there is a single ring. In contrast, dual and multiple rings are observed, if there are strong

Marangoni flows and stick-and-slip contact line motion during the evaporation. In order to obtain uniform dried patterns, the coffee-ring effect should be effectively suppressed. However, it is still difficult to obtain perfectly uniform particle patterns using evaporation of a droplet on a substrate due to the coffee-ring effect. To suppress this coffee-ring and to achieve uniformly deposited particle patterns, several ways were introduced; adding surfactants into droplets,[15] increasing the evaporation rate by the thermal effect,[16] changing the surface tension gradient by transfer of volatile vapors (*i.e.*, solutal Marangoni effect[17–20]), changing pH concentration,[21] controlling the elasticity and stiffness of the substrate[22–24] and using elongated ellipsoidal particles.[25] Most of the preceding studies on the uniform particle deposition are mainly done by applying additional chemical additives or external effects. However, the geometry effect on the dried pattern during evaporation has been rarely investigated.

There are some studies on evaporating droplets in a confined system. They simply observed the change of contact lines and contact angles under different geometrical conditions[26–29] and a final dried pattern was investigated between two parallel plates.[30,31] However, to date, studies of the final dried pattern inside the confined system have not been sufficiently done although some applications such as display diodes have a confined chamber containing quantum dots or other functional materials. In this sense, it is important to examine how a drop evaporates in a confined system and what kind of final dried pattern can be obtained.

If the droplet evaporates in a finite space, the ambient boundary conditions could be changed in time due to the evaporation of the droplet. The evaporated vapors will remain

Department of Mechanical Engineering, Korea Advanced Institute of Science and Technology, Daejeon 34141, Republic of Korea. E-mail: hshk@kaist.ac.kr; Fax: +82-042-350-3049; Tel: +82 042-350-3049

† Electronic supplementary information (ESI) available. See DOI: 10.1039/d0sm01872d

This journal is © The Royal Society of Chemistry 2021

in the confined area. Recently, some studies have demonstrated that changes in boundary conditions around a droplet directly influence an internal flow pattern inside the droplet during evaporation. For example, a neighboring droplet changes internal flow patterns inside an adjacent binary-mixture droplet.[32] Furthermore, external point sources of volatile vapors located near the droplet locally can generate Marangoni flows driven by surface tension gradient along a liquid–vapor interface inside a droplet[33,34] and also can control a particle distribution after the droplet is completely dried.[35] From these vapor-driven solutal Marangoni problems, we realized that the boundary conditions play an important role in changing internal flows and final dried patterns.

In this paper, we focus on the evaporation phenomenon of multi-component droplets composed of ethanol and distilled (DI) water in a confined geometry. We presume that evaporated vapors from the droplet remain in the confined chamber. The captured vapors stagnate around the droplet because the molecular weight of the volatile vapor component is much heavier than that of the ambient air.[36] We examine how the stagnant vapors affect internal flows inside the droplet during evaporation using particle image velocimetry (PIV). From PIV results, we found that stagnant volatile vapors induce all suspension particles to move towards the middle of the droplet and the particles gather with a circular shape, which is defined as particle accumulation. Also, we investigate flow transitions inside the droplet of multi-component solutions, *i.e.*, the binary or ternary mixture, under the confined conditions using PIV. We compare this result with an open system as well. Moreover, the uniformity of the final deposition patterns after the droplets completely dried in the confined chamber is examined in this study.

2 Experiments

2.1 Experimental set-up

In the experiment, we use a binary mixture droplet composed of ethanol ($\geq$99.5% purity, Sigma-Aldrich, USA.) and distilled (DI) water (Direct-Q3 UV, Sungwoo Genetech, Korea), which is widely used in a drying study.[37–40] As shown in Fig. 1, the droplet of the binary mixture is evaporated in a confined chamber fabricated by 3D printing (3DWOX 1, polylactic acid, Sindoh, Korea) at room temperature ($T \approx$ 293 K). Here, a 2 ± 0.04 μl droplet (V_o) is deposited on a cover glass and the radius R of the droplet is kept constant at around 1.5 mm by hydrophilic surface treatment using a plasma gun (BD-10ASV, Electro-Technic Products, INC., USA) with a shadow mask having a circular hole with R = 1.5 mm. The initial contact angle θ_o and droplet height h_o are $32 \pm 2°$ and 0.37 ± 0.01 mm, respectively. The confined chamber is completely sealed with a tape on top after placing the binary mixture droplet on the cover glass. Evaporated vapors are not allowed to diffuse out to the ambient environment due to the confined chamber so that the ethanol vapors are forced to remain in the chamber as sketched in Fig. 1.
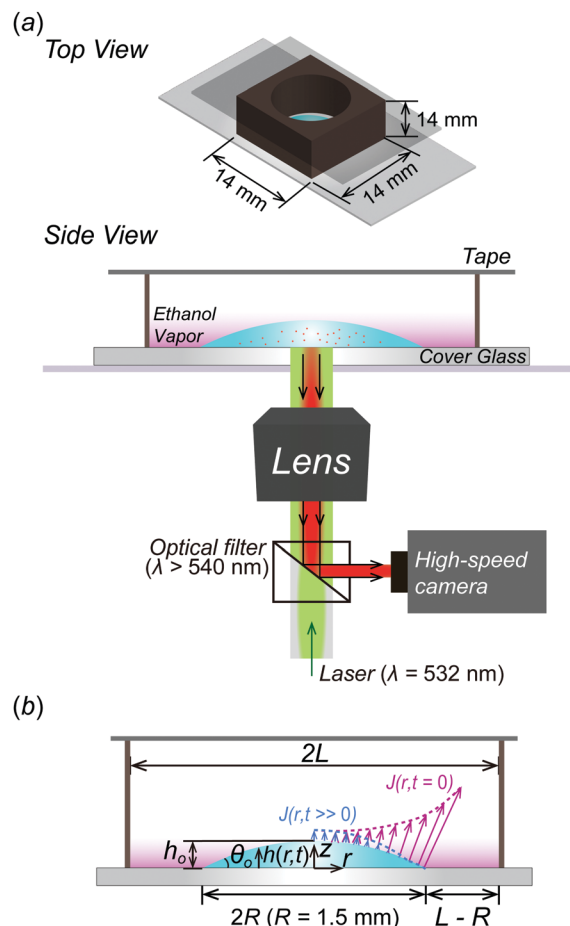

Fig. 1 (a) Schematic of the experimental setup for particle image velocimetry (PIV). To observe internal flow inside a binary-mixture droplet consisting of distilled (DI) water and ethanol, we use fluorescent particles. The fluorescence signal is excited at λ = 532 nm and emitted with λ = 607 nm. By using the optical filter (λ > 540 nm), the fluorescence signal is detected using a high-speed camera which is installed through a microscope. (b) A binary-mixture droplet with a constant radius R is deposited on a cover glass and confined by a 3D-printed structure with a circular hole and a tape. The size of the confined structure is 14 × 14 × 14 mm³ and diameter $2L$ for the inner hole. Pink gradation indicates that ethanol vapors evaporated from the droplet on the cover glass. The pink-dashed and light blue-dashed profile represent the evaporative flux of ethanol along the interface between liquid and vapor at t = 0 s and t > 0 s, respectively.

2.2 Flow visualization

To visualize internal flows inside droplets using particle image velocimetry (PIV), fluorescent particles (PS-FluoRed-Fi320, micro-particles GmbH, Germany) with a diameter of 1.9 ± 0.09 μm are used, whose concentration is 1% v/v in the binary mixture solution. Images of fluorescent particles during evaporation were recorded with 50 frames per second using a high-speed camera (Photron Fastcam Mini-AX200, Japan) and a 5× magnification lens. Also, the focal plane was set to the vicinity of the bottom part of the droplet where the depth of field is 150–200 μm from the substrate of the cover glass. Here, the droplet height h_o is much smaller than the droplet radius R ($h_o/R \approx 0.25 < 1$). Flow field calculation is conducted by the

Table 1 Physical properties (or vapor pressure or molecular weight) for solvents at $T \approx 293$ K

Solvent	Vapor pressure [kPa]	Molecular weight [g mol^{-1}]
Ethanol	5.95	46.07
Methanol[a]	13.02	32.04
1,4-Dioxane[b]	3.60	88.11
DI (distilled) water	2.34	18.02
Ambient air	—	28.93

[a] $\geq$99.9% purity, Sigma-Aldrich, USA. [b] $\geq$99.8% purity, Sigma-Aldrich, USA.

PIVlab tool in Matlab.[41] To obtain vector fields, we apply iterative 2D cross-correlation of the particle images with multiple interrogation windows of 128×128 pixels (first) and 64×64 pixels (second) with 50% overlaps, where the signal-to-noise ratio (SNR > 3) is large enough for the reliable PIV.[42]

2.3 Deposition patterns

We evaluated uniformity of dried patterns after a completed evaporation in the confined geometry with various combinations of solvents [see Table 1]. All the solvents used in this experiment are much more volatile than DI-water and have heavier molecular weight than the ambient air as listed in Table 1. Not only fluorescent particles, but also greenish quantum dots (CZM-530W QDs, ZEUS, Korea) were tested whether a surface-coating method newly proposed in this paper can obtain a uniform pattern. Eventually, it can be utilized in relevant applications, such as light-emitting devices,[43] solar cells[44] and color filters in displays.[45–47] In the experiment, water-soluble QDs with a particle concentration of 5 mg ml^{-1} in water and a size of 10.5 ± 1.5 nm are used where they can emit light in the $\lambda = 450$ nm wavelength range with full width at half maximum (FWHM) $\leq$35 nm when they are exposed to ultraviolet rays (Photo Luminescence, PL) or current (Electron Luminescence, EL). QD particles are stably dispersed in the solution with ζ-potential -20 to -40 mV. In this study, the final deposition of QDs was visualized by using an ultraviolet ray lamp (PL) where we mixed ethanol, DI-water and QDs with weight ratio, 44.1% : 55.7% : 0.2% in the solution.

3 Results and discussion

3.1 Theoretical background

In this study, during the experiment, ethanol evaporation is relatively predominant compared to water because the vapor pressure of ethanol ($P_v = 5.95$ kPa) is about 2 times higher than that of water ($P_v = 2.34$ kPa). Thus, we mainly consider an evaporative flux of the ethanol along an air–liquid interface, which varies with space (r) and time (t) due to the confinement effect. In this problem, initially, $h(r, t = 0, 0)/R < 1$ and $h(r, t)/R$ become smaller as the droplet evaporates so that we can use lubrication approximation for a thin droplet. As a result, the

evaporative flux can be expressed as follows[48–51]

$$J_{\text{EtOH}} \cong \frac{2D_{\text{va}}\Delta C}{\pi \sqrt{R^2 - r^2}} \tag{1}$$

where $D_{\text{va}} \approx 1.1 \times 10^{-5}$ m^2 s^{-1} is the diffusivity of the ethanol vapor and $\Delta C = C_s(1 - H_R) = C_s - C_e$ where C_s is the saturation ethanol vapor concentration (0.159 kg m^{-3} at $T \approx 300$ K), C_e is an ethanol vapor concentration around the droplets, and H_R is the relative ethanol concentration (%) between a liquid and a surrounding environment.

Here, in the case of evaporation for an open substrate, ethanol vapor concentration C_e might be constant (here, $C_e \approx 0$) because the ethanol vapors can freely discharge into the ambient atmosphere in a relatively infinite area. In other words, if they are not constrained by geometries, the ethanol vapor concentration gradient could be constant, i.e. ($\Delta C = C_s - C_e \approx C_s$). However, in a confined system, evaporated ethanol vapors cannot diffuse out to the ambient environment due to the fabricated confined chamber and they stagnate in the chamber where the molecular weight of ethanol ($M_{\text{EtOH}} = 46.07$ g mol^{-1}) is much heavier than the ambient air ($M_{\text{air}} = 28.93$ g mol^{-1}), so the vapors sink down to the bottom direction, as shown in the pink gradation in Fig. 1. Simultaneously, the stagnant ethanol vapors result in an increase of ethanol vapor concentration C_e in the vicinity of the droplet. Consequently, the ethanol vapor concentration gradient diminishes as the droplet evaporates, i.e. ($\Delta C = C_s - C_e$), which induces a decreased evaporative flux profile based on the following relational formula,

$$\vec{J}_{\text{EtOH}}(\vec{r}, t) \propto C_s - C_e(\vec{r}, t). \tag{2}$$

In a confined system, as the ethanol vapor concentration ΔC along a droplet surface changes, the evaporative flux profile J varies based on eqn (1) and (2). At the same time, the surface tension gradient along a liquid–vapor interface also changes with space and time. Consequently, time-dependent Marangoni flows inside the droplets in the confined system would be differently developed compared to the experimental results of the open substrate.

3.2 Flow field

To investigate the internal flow pattern, we perform PIV and the results are summarized in Fig. 2. We find that the internal flows of binary mixture (ethanol : DI-water = 70 : 30 vol%) in a confined chamber can be classified into three stages: Stage I, complicated Marangoni-driven convection flow, Stage II, continuous inward flow, and Stage III, gradually diminishing Marangoni flow as shown in Fig. 2(b). At stage I, complicated mixing flows are observed everywhere inside the droplet, which is a similar result to initial evaporative flow patterns on an open substrate [Fig. 2(a and b)], where the typical flow speed $U \approx O(0.1 \text{ mm s}^{-1})$. At stage II, the inward circulation flow pattern is developed and maintained for longer time compared to the droplet on an open substrate (see the ESI,† Movies S1 and S2). The long-lasting inward circulation flows in the confined chamber is due to stagnant ethanol vapors around
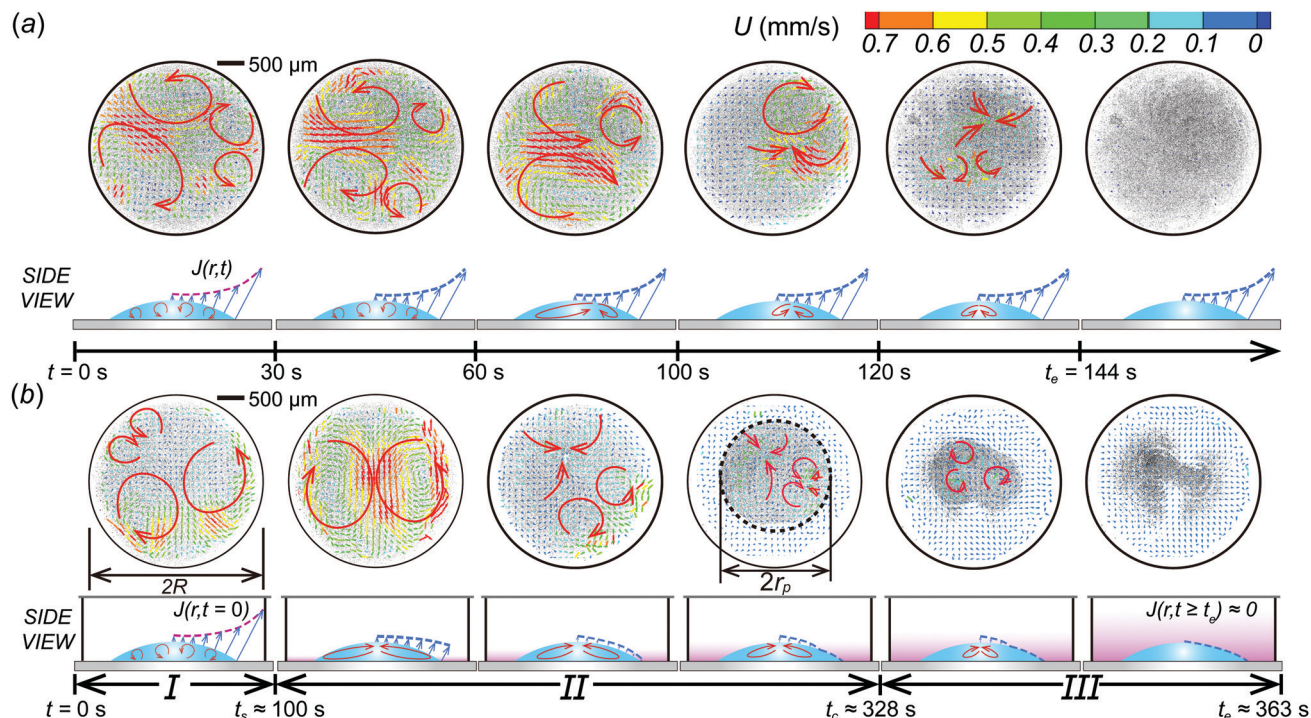
Fig. 2 Comparison of internal flow fields of an ethanol–water (70 : 30 vol%) mixture droplet on (a) an open and in (b) a confined geometry. (a) A mixture droplet evaporation on a substrate. Initially, complicated Marangoni-driven convection flow is dominant. As time goes, the Marangoni flows gradually disappear and stop at $t = t_e$ (here, 144 s) on an open system. (b) In a confined geometry, Stage I: complicated Marangoni-driven convection flow is shown. Stage II: all suspended particles (black dots) begin to be accumulated in the middle of the droplet due to solutal Marangoni effects and we observed that the critical radius r_p (green-dashed line) is developed at $t = t_c$ (here, 328 s). Stage III: Marangoni flows gradually become weaker as the ethanol continuously evaporates. At $t = t_e$ (here, 363 s), the internally circulating convective flow almost stops. Pink gradation shows stagnant ethanol vapors around the droplet surface over time. $J(r,t)$ represents an evaporative flux along the liquid–vapor interface over time. At $t = 0$, $J(r,t)$ shows a purple-dashed profile. The blue-dashed profile indicates estimated evaporative flux $J(r,t)$ for $t > 0$ during evaporation.

droplets that can continuously generate a surface tension gradient at a liquid–vapor interface, which contributes to the development of Marangoni flow inside droplets in a confined system for a much longer period of time than that of the open system. The typical inward flow induces particle accumulation in the middle of the droplet, which forms a certain circular area with the smallest radius r_p at $t_c \approx 328$ s in Fig. 2(b). We defined the smallest radius r_p as a critical radius in this study. At stage III, Marangoni flow inside the droplet is gradually diminished as the ethanol components in the droplet evaporate.

If the droplet evaporates on an open substrate, complicated mixing flows are observed in the beginning of evaporation. When ethanol completely evaporates, the mixing flows stop and it shows a coffee-ring flow pattern. For the open system, the time duration of the mixing flow regime is relatively shorter than the confined system ($t \approx 60$ s). From PIV results, we see that the confinement effect can obviously change the flow structure in time and in space. Hereby, we conclude that the confined system changes the boundary condition related to the evaporation mechanism.

3.3 Effect of stagnant ethanol vapors

To further investigate the particle accumulation phenomenon, we control an initial ethanol concentration C_{EtOH} in a droplet and a distance $L-R$ between the droplet and inner walls and

initial droplet height h_o. Fig. 3(a) shows that the critical radius r_p decreases as the ethanol concentration C_{EtOH} inside the droplet increases from 30 to 50 and 70% with a volume ratio in the droplet. The reason is that the amount of ethanol vapors around the droplet increases with the ethanol concentration so that it helps to make long-lasting continuous inward flow, which plays a role in accumulating all suspended particles in the middle of the droplet.

We have shown that the ethanol concentration is proportional to the duration of Marangoni flow, which can help to concentrate the particles in the middle further. In a similar manner, we consider the relation between the amount of the evaporated volatile liquid vapors and the chamber space. To examine this, we varied the $L-R$ space. As shown in Fig. 3(b), we noticed that distance $L-R$ is also an important factor to determine the critical radius r_p. From the result, the minimal radius r_p is observed with $L-R = 1.5$ mm. This indicates that there is an optimized chamber size to achieve the long-lasting Marangoni flow condition. On the other hand, for $L-R = 0.5$ mm [blue-shaded area in Fig. 3(b)], if the space between the droplet and solid inner wall is relatively small, the ethanol vapor can easily and uniformly cover the entire droplet so that the Marangoni effect caused by a surface tension gradient at a droplet surface rapidly disappears and it cannot make smaller r_p. Actually, the duration time of the inward circulation flow is $t_e \approx 36$ s for
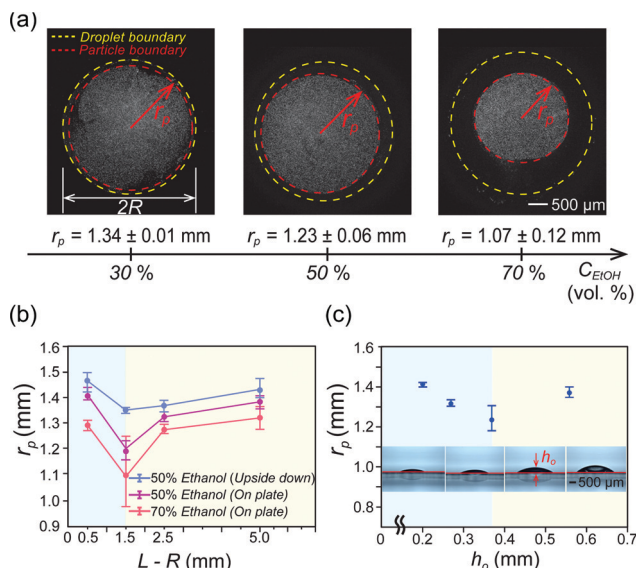
Fig. 3 Comparison of particle accumulation by Marangoni flow by varying different ethanol concentrations and geometry conditions. (a) Images of the particle distribution region in the binary mixture droplet with 30, 50, and 70% ethanol concentration C_{EtOH} in water, respectively. Initial droplet diameters are the same as $2R$. The critical radius r_p is defined when all the particles are gathered in the smallest region (red-dashed line). (b) Effect of the distance $L-R$ (see Fig. 1(b)) between the wall and the droplet with ethanol–water (50 : 50 vol%) and ethanol–water (70 : 30 vol%) (purple and orange line) on the critical radius r_p. The blue line is for the upside down droplet case. (c) Effect of initial droplet height h_o (0.5, 1, 2, and 3 µl volume of the droplet) on critical radius r_p. Here, the initial contact angle θ_o and droplet height h_o are measured as $20 \pm 1°$ and 0.20 ± 0.01 mm for a 0.5 µl drop, $23 \pm 2°$ and 0.28 ± 0.01 mm for 1.0 µl, $32 \pm 2°$ and 0.37 ± 0.01 mm for 2.0 µl and $37 \pm 2°$ and 0.56 ± 0.01 mm for 3.0 µl, respectively.

$L-R$ = 0.5 mm for an ethanol concentration C_{EtOH} = 50 vol% in water. However, the duration time for internal circulation flows also increases as $L-R$ increases because they are less likely to be covered by the stagnant ethanol vapors due to a large area ($L-R$ = 1.5 mm: $t_e \approx$ 180 s, $L-R$= 2.5 mm: $t_e \approx$ 330 s, $L-R$ = 5.0 mm: $t_e \approx$ 380 s). Also, as $L-R$ gradually increases [the yellow-shaded area in Fig. 3(b)], the confinement effects on the droplet evaporation become weaker by losing the surface tension gradient along the droplet interface as the ethanol evaporates. Thus, the critical radius r_p increases.

In addition, to prove the gravity effect due to the density difference between an ethanol vapor and ambient air, we measure and compare critical radius r_p for sessile and upside down droplet evaporation in a confined system. We expect that the larger critical radius r_p will be obtained if the droplet is placed under the substrate because a molecular weight of ethanol vapors is much heavier than that of the ambient air so that the ethanol vapors leave away from the droplet surface. From the experimental result [blue line in Fig. 3], in the case of upside down, they have larger critical radius r_p than other cases. From this, we can conclude that the evaporated ethanol vapors sink down onto the bottom by the gravity effect driven by the density difference and, therefore, the inversely suspended droplet does not have a strong Marangoni effect during evaporation.

Moreover, in order to check the effect of a droplet height on critical radius r_p, we control a droplet volume, 0.5, 1.0, 2.0 and 3.0 µl in the same confined chamber [see insets in Fig. 3(c)] while fixing the constant radius R and the same initial concentration of ethanol in the droplet (R = 1.5 mm and ethanol 50% in water with a volume ratio). We found that a critical condition is $h_o \approx$ 0.37 mm (2 µl droplet) in Fig. 3(c) to distinguish two regimes. First, in the blue-shaded area, they have relatively very shallow droplet height h_o so that they can be easily covered by an stagnant ethanol vapor within a short moment and then Marangoni flows inside the droplet cannot be continued for a long time (actually, $t_e \approx$ 60–80 s). Eventually, relatively larger critical radius r_p is observed [blue-shaded area in Fig. 3(c)]. On the other hand, in the yellow-shaded area, this case has a sufficient droplet height not to be easily covered with the ethanol vapors and there is an enough space for the evaporated ethanol vapors diffused into the ambient environment. Therefore, under the same conditions, as the droplet height h_o increases, the contact angle gets larger. Then, the influenced area near the contact line becomes narrower so that the larger critical radius r_p is developed as shown in the yellow-shaded area in Fig. 3(c). We found that the optimal conditions for the smallest r_p are for $h_o \approx$ 0.37 mm (a droplet volume 2 µl) and $L-R$ is 1.5 mm. In this study, we find the droplet height $h_o \approx$ 0.37 mm is an optimal condition for minimal critical radius r_p.

As a result, we observe that there is an optimal condition to have a long-lasting Marangoni flow and a smaller r_p, which can be determined by the concentration of the evaporated vapors, the confinement space, and the droplet shape.

3.4 Results of the deposition pattern

As shown in Fig. 4(a), we compare dried patterns in a confined chamber by using various solvents; ethanol, methanol, 1,4-dioxane and DI-water. The dried patterns of binary (A–C) and ternary (D) solution that consist of the abovementioned solvents. We observed that (A–D) shows uniformly distributed particle patterns compared to the coffee-ring pattern produced by evaporation of pure water (E) in Fig. 4. To quantitatively compare the uniformity, we measured the averaged particle image density as a function of the radial direction and the result can clearly show uniformly deposited patterns [Fig. 4(b)]. The intensity profile $I(r)$ is normalized with the maximum I_{max} where $I(r) = (1/2\pi)\int_0^{2\pi} i(r,\theta)d\theta$ and $i(r,\theta)$ is the local light intensity.

The procedure of drying of the droplet in a confined chamber is summarized in Fig. 4(c). Initially ($0 \leq t \leq t_e$), all suspended particles congregate towards the center of the droplet due to inward Marangoni flows in the middle of the droplet induced by evaporated ethanol vapors stagnant near the droplet [see also Fig. 2b], where t_e is the final time for the Marangoni flow to disappear. After that ($t_e < t$), the ethanol vapor concentration near the droplet surface, is saturated by stagnant ethanol vapors and gathered particles in the middle of the droplet start to spread out towards the contact line because the strong Marangoni flow disappears.
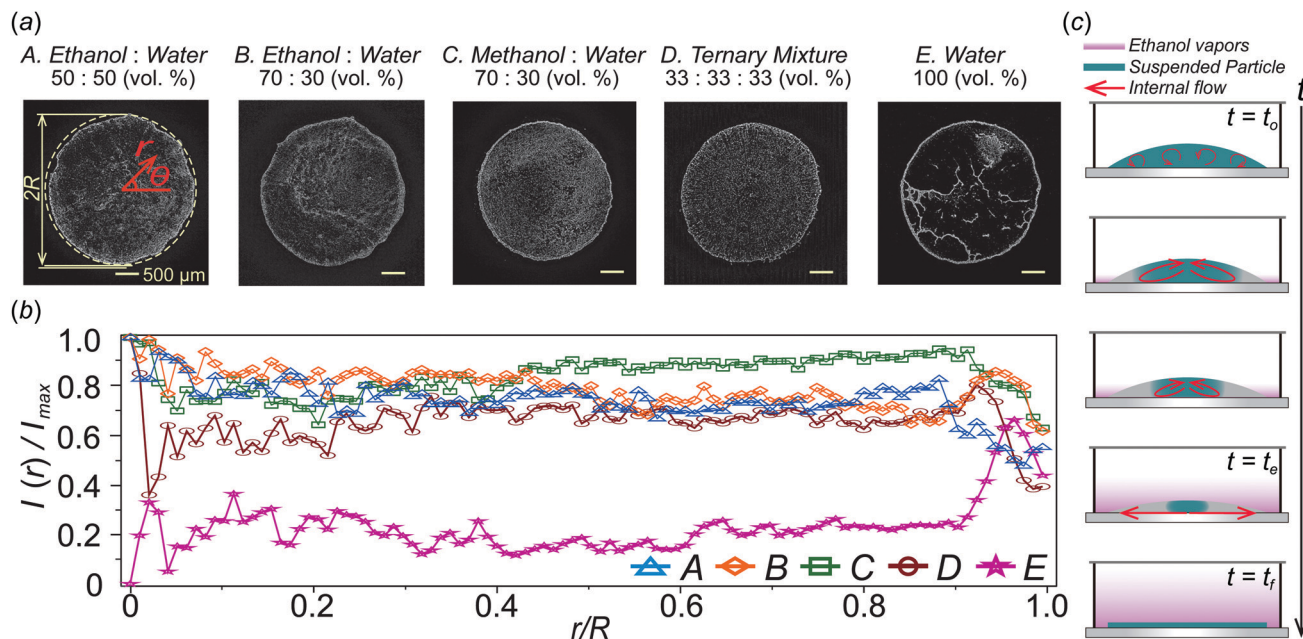
Fig. 4 Comparison of deposition patterns with different solution components. (a) Images of deposition patterns: (A) ethanol : water = 50 : 50 (vol%), (B) ethanol : water = 70 : 30 (vol%), (C) methanol : water = 70 : 30 (vol%), (D) ethanol : water : 1,4-dioxane = 33 : 33 : 33 (vol%), and (E) water = 100 (vol%). Diameter of the deposition is $2R$. (b) The intensity profile $I(r)$ normalized with the maximum I_{max} where $I(r) = (1/2\pi)\int_0^{2\pi} i(r, \theta)\mathrm{d}\theta$ and $i(r,\theta)$ is the local light intensity. (c) Drying processes of a droplet in a confined system where t_o is the time at which evaporation of droplets starts, t_e is the time until all suspended particles are accumulated in the middle of the droplet by continuous inward flows and the flows almost disappear, and t_f is the time when the droplet is completely dried.

However, the ethanol vapors next to the droplet surface help to suppress the coffee-ring pattern by vapor-driven solutal Marangoni effects.[33,34] Finally, we can achieve relatively uniform deposition without coffee-ring patterns [Fig. 4(a) and (b)].
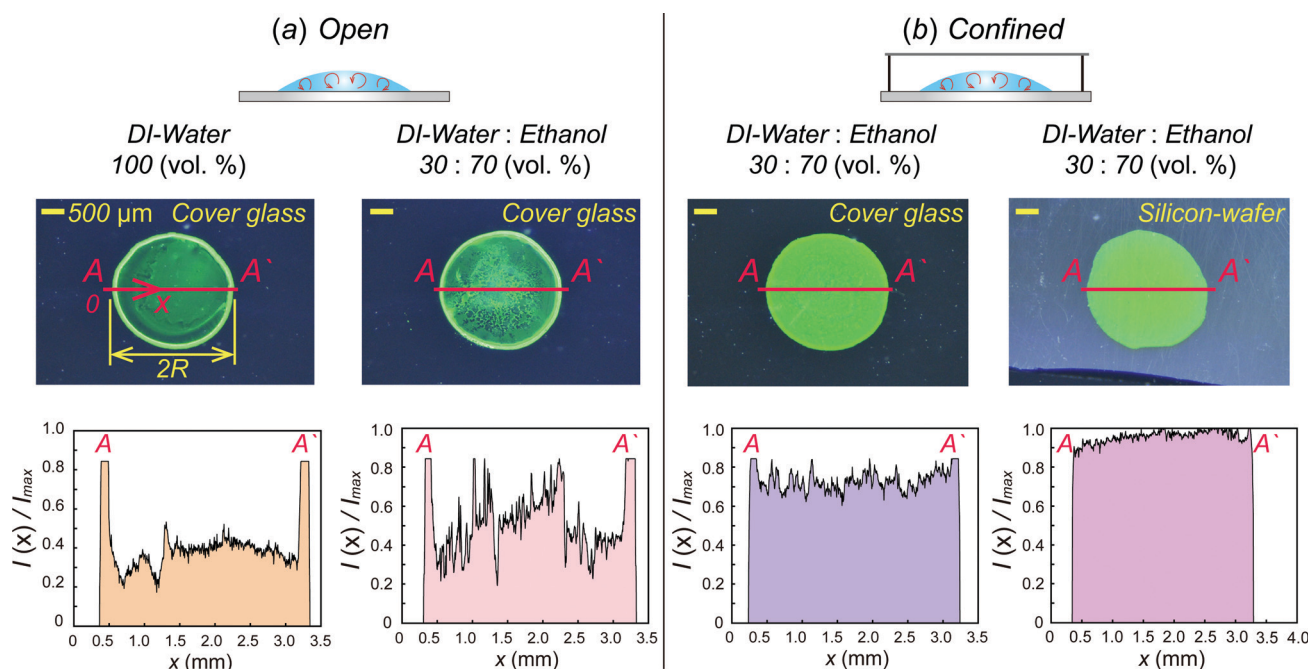

Fig. 5 Comparison of water-soluble QDs deposition patterns with different conditions; an (a) open and (b) confined space. (a) Image of water-soluble QD deposition patterns on a cover glass and corresponding intensity profiles $I(x)$ normalized with I_{max} for pure DI-water and binary mixture (ethanol : DI-water = 70 : 30 vol%) on open substrates. (b) Water-soluble QD deposition patterns and corresponding intensity profiles $I(x)$ normalized with I_{max} for binary mixture (ethanol : DI-water = 70 : 30 vol%) deposited on a cover glass and silicon−wafer, respectively, in the confined geometry. Solutions are prepared as DI-water : QDs = 99.9 : 0.1 wt% for pure DI-water and ethanol : DI-water : QDs = 44.1 : 55.7 : 0.2 wt% for the binary mixture.

For a real application, we use water-soluble QDs as a coating material. As shown in Fig. 5, uniform surface-coating was obtained where the solvent consists of ethanol, DI-water and QDs with weight ratio; 44.1% : 55.7% : 0.2%, respectively, while the coffee-ring pattern is clearly formed when a DI-water or binary mixture droplet evaporates in an open system [Fig. 5(a)]. We test two different substrates as a potential substrate. There is a slight difference between two cases (*i.e.*, glass and silicon-wafer) from the intensity distribution. However, the illumination results excited by UV light (λ = 395 nm) provide a uniform green color everywhere [Fig. 5(b)]. We believe that the current method would be a reliable QD printing method for a display element.

4 Conclusions

We investigate how a multi-component liquid droplet evaporates in a confined chamber and we observe a final deposit pattern. As a consequence, uniformly dried patterns are achieved using the proposed method. To understand this result, by using the PIV technique, we monitor and compare internal flow fields between droplet evaporation on an open substrate and in a confined system. It is confirmed that long-lasting continuous inward circulation flows in the middle of the droplet generate in the confined chamber and these flows play a leading role in inducing the particle accumulation phenomenon. Eventually, we obtain uniform dried patterns without the coffee-ring. For some specific patterning, the evaporation in the confined system based on ink-jet printing is commonly used when color filters are manufactured in display fields.[52,53] Then, it is crucial that uniform surface-coating technologies are still required for high luminous quality and efficiency. Therefore, to check the potential of the proposed method for being applicable to practical applications, we also test QDs deposition patterns and obtain uniformly illuminated spots on two different substrates, *i.e.*, a cover glass and silicon–wafer. We expect that the proposed surface-coating method can be widely applied in various relevant industrial areas without any external energy sources and adding special additives to achieve uniform coating with a restrained coffee-ring effect.

Conflicts of interest

There are no conflicts to declare.

References

1 B.-J. De Gans, P. C. Duineveld and U. S. Schubert, *Adv. Mater.*, 2004, **16**, 203–213.

2 Y. L. Kong, I. A. Tamargo, H. Kim, B. N. Johnson, M. K. Gupta, T.-W. Koh, H.-A. Chin, D. A. Steingart, B. P. Rand and M. C. McAlpine, *Nano Lett.*, 2014, **14**, 7017–7023.

3 B. Chen, T. Cui, Y. Liu and K. Varahramyan, *Solid-State Electron.*, 2003, **47**, 841–847.

4 E. B. Secor, P. L. Prabhumirashi, K. Puntambekar, M. L. Geier and M. C. Hersam, *J. Phys. Chem. Lett.*, 2013, **4**, 1347–1351.

5 L. Yang, A. Rida, R. Vyas and M. M. Tentzeris, *IEEE Trans. Microwave Theory Tech.*, 2007, **55**, 2894–2901.

6 X. Cui and T. Boland, *Biomaterials*, 2009, **30**, 6221–6227.

7 T. Xu, W. Zhao, J.-M. Zhu, M. Z. Albanna, J. J. Yoo and A. Atala, *Biomaterials*, 2013, **34**, 130–139.

8 X. Yu, R. Xing, Z. Peng, Y. Lin, Z. Du, J. Ding, L. Wang and Y. Han, *Chin. Chem. Lett.*, 2019, **30**, 135–138.

9 C. Jiang, Z. Zhong, B. Liu, Z. He, J. Zou, L. Wang, J. Wang, J. Peng and Y. Cao, *ACS Appl. Mater. Interfaces*, 2016, **8**, 26162–26168.

10 R. Singh, E. Singh and H. S. Nalwa, *RSC Adv.*, 2017, **7**, 48597–48630.

11 R. D. Deegan, O. Bakajin, T. F. Dupont, G. Huber, S. R. Nagel and T. A. Witten, *Nature*, 1997, **389**, 827–829.

12 X. Zhong and F. Duan, *Phys. Chem. Chem. Phys.*, 2016, **18**, 20664–20671.

13 M. Parsa, S. Harmand, K. Sefiane, M. Bigerelle and R. Deltombe, *Langmuir*, 2015, **31**, 3354–3367.

14 L. Shmuylovich, A. Q. Shen and H. A. Stone, *Langmuir*, 2002, **18**, 3441–3445.

15 H. Kim, F. Boulogne, E. Um, I. Jacobi, E. Button and H. A. Stone, *Phys. Rev. Lett.*, 2016, **116**, 124501.

16 Y. Li, Q. Yang, M. Li and Y. Song, *Sci. Rep.*, 2016, **6**, 1–8.

17 S. Bekki, M. Vignes-Adler, E. Nakache and P. Adler, *J. Colloid Interface Sci.*, 1990, **140**, 492–506.

18 C. Sternling and L. Scriven, *AIChE J.*, 1959, **5**, 514–523.

19 K. Schwarzenberger, T. Köllner, H. Linde, T. Boeck, S. Odenbach and K. Eckert, *Adv. Colloid Interface Sci.*, 2014, **206**, 344–371.

20 M. Majumder, C. S. Rendall, J. A. Eukel, J. Y. Wang, N. Behabtu, C. L. Pint, T.-Y. Liu, A. W. Orbaek, F. Mirri and J. Nam, *et al.*, *J. Phys. Chem. B*, 2012, **116**, 6536–6542.

21 R. Bhardwaj, X. Fang, P. Somasundaran and D. Attinger, *Langmuir*, 2010, **26**, 7833–7842.

22 R. Iqbal, A. Matsumoto, A. Sudeepthi, A. Q. Shen and A. Sen, *Appl. Phys. Lett.*, 2019, **114**, 253701.

23 Y. Chen, A. Askounis, V. Koutsos, P. Valluri, Y. Takata, S. K. Wilson and K. Sefiane, *Langmuir*, 2019, **36**, 204–213.

24 M. C. Lopes and E. Bonaccurso, *Soft Matter*, 2013, **9**, 7942–7950.

25 P. J. Yunker, T. Still, M. A. Lohr and A. Yodh, *Nature*, 2011, **476**, 308–311.

26 L. Bansal, S. Chakraborty and S. Basu, *Soft Matter*, 2017, **13**, 969–977.

27 J. Li, L. Shan, B. Ma, X. Jiang, A. Solomon, M. Iyengar, J. Padilla and D. Agonafer, *J. Colloid Interface Sci.*, 2019, **555**, 583–594.

28 F. Clément and J. Leng, *Langmuir*, 2004, **20**, 6538–6541.

29 J. Leng, *Phys. Rev. E: Stat., Nonlinear, Soft Matter Phys.*, 2010, **82**, 021405.

30 P. J. Yunker, M. Gratale, M. A. Lohr, T. Still, T. C. Lubensky and A. G. Yodh, *Phys. Rev. Lett.*, 2012, **108**, 228303.

31 R. Mondal and M. G. Basavaraj, *Soft Matter*, 2020, **16**, 3753–3761.

32 T. K. Pradhan and P. K. Panigrahi, *Colloids Surf., A*, 2016, **500**, 154–165.

33 J. Ryu, J. Kim, J. Park and H. Kim, *Int. J. Heat Mass Transfer*, 2021, **164**, 120499.

34 J. Park, J. Ryu, H. J. Sung and H. Kim, *J. Colloid Interface Sci.*, 2020, **561**, 408–415.

35 R. Malinowski, G. Volpe, I. P. Parkin and G. Volpe, *J. Phys. Chem. Lett.*, 2018, **9**, 659–664.

36 P. Kelly-Zion, C. J. Pursell, N. Hasbamrer, B. Cardozo, K. Gaughan and K. Nickels, *IInt. J. Heat Mass Transfer*, 2013, **65**, 165–172.

37 J. R. Christy, Y. Hamamoto and K. Sefiane, *Phys. Rev. Lett.*, 2011, **106**, 205701.

38 C. H. Ooi, E. Bormashenko, A. V. Nguyen, G. M. Evans, D. V. Dao and N.-T. Nguyen, *Langmuir*, 2016, **32**, 6097–6104.

39 X. Zhong and F. Duan, *Eur. Phys. J. E: Soft Matter Biol. Phys.*, 2016, **39**, 1–6.

40 C. Diddens, H. Tan, P. Lv, M. Versluis, J. Kuerten, X. Zhang and D. Lohse, *J. Fluid Mech.*, 2017, **823**, 470–497.

41 W. Thielicke and E. Stamhuis, *J. Open Res.*, 2014, **2**.

42 L. Adrian, R. J. Adrian and J. Westerweel, *Particle Image Velocimetry*, Cambridge University Press, 2011.

43 Y. Shirasaki, G. J. Supran, M. G. Bawendi and V. Bulović, *Nat. Photonics*, 2013, **7**, 13.

44 Z. Yang, M. Wang, J. Li, J. Dou, H. Qiu and J. Shao, *ACS Appl. Mater. Interfaces*, 2018, **10**, 26387–26395.

45 J. Han, D. Ko, M. Park, J. Roh, H. Jung, Y. Lee, Y. Kwon, J. Sohn, W. K. Bae and B. D. Chin, *J. Soc. Inf. Disp.*, 2016, **24**, 545–551.

46 B. Bao, M. Li, Y. Li, J. Jiang, Z. Gu, X. Zhang, L. Jiang and Y. Song, *Small*, 2015, **11**, 1649–1654.

47 P. Yang, L. Zhang, D. J. Kang, R. Strahl and T. Kraus, *Adv. Opt. Mater.*, 2020, **8**, 1901429.

48 R. D. Deegan, O. Bakajin, T. F. Dupont, G. Huber, S. R. Nagel and T. A. Witten, *Phys. Rev. E: Stat., Nonlinear, Soft Matter Phys.*, 2000, **62**, 756.

49 H. Hu and R. G. Larson, *J. Phys. Chem. B*, 2002, **106**, 1334–1344.

50 Y. O. Popov, *Phys. Rev. E: Stat., Nonlinear, Soft Matter Phys.*, 2005, **71**, 036313.

51 H. Gelderblom, A. G. Marin, H. Nair, A. Van Houselt, L. Lefferts, J. H. Snoeijer and D. Lohse, *Phys. Rev. E: Stat., Nonlinear, Soft Matter Phys.*, 2011, **83**, 026306.

52 H.-S. Koo, M. Chen and P.-C. Pan, *Thin Solid Films*, 2006, **515**, 896–901.

53 C.-T. Chen, K.-H. Wu, C.-F. Lu and F. Shieh, *J. Micromech. Microeng.*, 2010, **20**, 055004.